Author Manuscript

Author Manuscript

Author Manuscript

Author Manuscript

HHS Public Access

Author manuscript

Cell Rep Phys Sci. Author manuscript; available in PMC 2024 November 07.

Published in final edited form as:

Cell Rep Phys Sci. 2024 October 16; 5(10): . doi:10.1016/j.xcrp.2024.102211.

Manipulating the molecular specificity of transcriptional biosensors for tryptophan metabolites and analogs

Chenggang Xi[1,4], **Yuefeng Ma**[1,4], **Matthew B. Amrofell**[1], **Tae Seok Moon**[1,2,3,5,6,*]

[1]Department of Energy, Environmental and Chemical Engineering, Washington University in St. Louis, St. Louis, MO, USA

[2]Division of Biology and Biomedical Sciences, Washington University in St. Louis, St. Louis, MO, USA

[3]Synthetic Biology Group, J. Craig Venter Institute, La Jolla, CA, USA

[4]These authors contributed equally

[5]X (formerly Twitter): @Moon_Synth_Bio

[6]Lead contact

SUMMARY

Tryptophan and its metabolites, produced by the gut microbiota, are pivotal for human physiological and mental health. Yet, quantifying these structurally similar compounds with high specificity remains a challenge, hindering point-of-care diagnostics and targeted therapeutic interventions. Leveraging the innate specificity and adaptability of biological systems, we present a biosensing approach capable of identifying specific metabolites in complex contexts with minimal cross-activity. This study introduces a generalizable strategy that combines evolutionary analysis, key ligand-binding residue identification, and mutagenesis scanning to pinpoint ligand-specific transcription factor variants. Furthermore, we uncover regulatory mechanisms within uncharacterized ligand-binding domains, whether in homodimer interfaces or monomers, through structural prediction and ligand docking. Notably, our “plug-and-play” strategy broadens the detection spectrum, enabling the exclusive biosensing of indole-3-acetic acid (an auxin), tryptamine, indole-3-pyruvic acid, and other tryptophan derivatives in engineered probiotics. This groundwork paves the way to create highly specific transcriptional biosensors for potential clinical, agricultural, and industrial use.

This is an open access article under the CC BY-NC-ND license (http://creativecommons.org/licenses/by-nc-nd/4.0/).

*Correspondence: tsmoon7@gmail.com.

AUTHOR CONTRIBUTIONS

Conceptualization, T.S.M.; resources, T.S.M.; methodology, C.X., Y.M., and M.B.A.; validation, C.X., Y.M., and M.B.A.; investigation, C.X., Y.M., and M.B.A.; data curation, C.X. and Y.M.; formal analysis, C.X.; visualization, C.X.; writing – original draft, C.X.; writing – review & editing, C.X. and T.S.M.; supervision, C.X. and T.S.M.; project administration, T.S.M.; funding acquisition, T.S.M.

DECLARATION OF INTERESTS

A patent has been filed (US Patent Application No. 17/731195).

SUPPLEMENTAL INFORMATION

Supplemental information can be found online at https://doi.org/10.1016/j.xcrp.2024.102211.

Author Manuscript Author Manuscript Author Manuscript Author Manuscript

Graphical Abstract

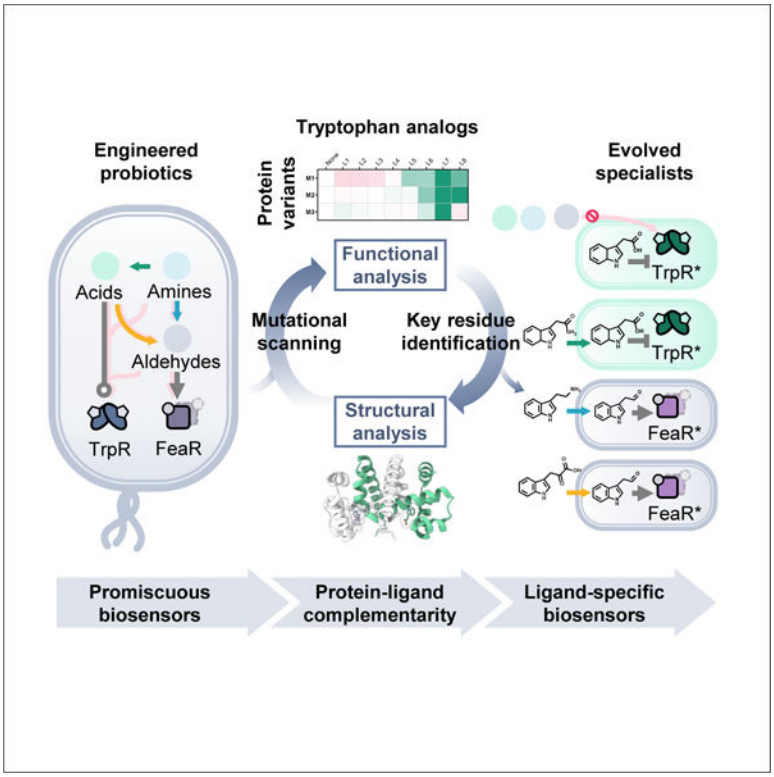

Xi et al. use synthetic biology tools to enhance transcriptional biosensor specificity and reveal key allosteric mechanisms, minimizing signal crosstalk in tryptophan or auxin metabolism pathways. This approach couples biosensing elements with various enzymes, providing detection and regulation tools with high orthogonality for industrial, agricultural, or biomedical applications.

INTRODUCTION

Tryptophan (TRP), an essential amino acid, is transformed by human cells and microbiota into a vast array of indole derivatives, pivotal for human health and host-microbe communication.[1–3] Gut-microbial metabolites derived from dietary TRP are of significant interest due to their profound impact on modulating the immune system, enhancing gut barrier functionality, and interacting with the central nervous system via the gut-brain axis.[4–6] Notably, indole-3-acetic acid (IAA; also an auxin or a plant hormone) and indole carboxaldehyde (IAld) engage with aryl hydrocarbon receptors (AhRs) on intestinal epithelial and immune cells, regulating immune responses and fortifying the intestinal barrier.[7–9] Likewise, indole-3-propionic acid (IPA) is another microbiota-derived TRP metabolite with significant antioxidant and anti-inflammatory properties, protecting against oxidative stress.[7,10] It is also linked to blood-brain barrier integrity and is associated with a reduced risk of type 2 diabetes.[11,12] Furthermore, several gut-microbial TRP metabolites, including tryptamine (TRM), serotonin (5-hydroxytryptamine; 5HT), and melatonin, possess neuroactive properties.[4] These compounds underscore the substantial influence of the gut microbiome on gastrointestinal (GI) functionality and mental health.

Author Manuscript Author Manuscript Author Manuscript Author Manuscript

Despite their chemical resemblance, TRP-related compounds fulfill vastly different roles in human health, and imbalances in TRP metabolites caused by gut-microbial dysbiosis can disrupt GI tract function.[13,14] For instance, TRM secreted by commensal bacteria could crosstalk with both 5HT G-protein-coupled receptor and AhR in the intestinal epithelium, while IAA and IAld could only interact with AhR.[2,15] Recent findings highlight IAA's potential to enhance cancer therapy effectiveness, a property not observed with IPA.[16] Similarly, IPA and its precursor indole-3-acrylic acid have been proven to modulate inflammatory responses differently in the gut.[10] Consequently, precise quantification of these compounds is crucial for the diagnosis and prevention of digestive and mental disorders. However, the structural similarities and diversity among TRP metabolites complicate their monitoring and regulation within gut environments. Traditional analytical methods such as high-performance liquid chromatography (HPLC), mass spectrometry, or NMR involve extensive sample preparation and data analysis for *in vitro* quantification,[7] while current biosensing methods are incapable of detecting these chemicals with high specificity and sensitivity.[17]

Transcriptional biosensors have become integral to metabolic engineering and the development of living diagnostics and therapeutics.[18–20] Although these biosensors are renowned for their high specificity toward target effectors, their ability to bind multiple structurally similar compounds introduces a degree of promiscuity.[21,22] Both enzyme and regulator promiscuity can lead to complex crosstalk in metabolic engineering, hindering the dynamic regulation of specific metabolites.[23,24] In biomedical contexts, the nonspecific detection of disease biomarkers is particularly problematic, raising the risk of misdiagnosis and incorrect treatment.[25,26]

In this work, we have engineered transcription factors (TFs) TrpR and FeaR for the exclusive detection of IAA and indole-3-acetaldehyde (IAAld) in probiotic *Escherichia coli* Nissle 1917 (EcN) through semi-rational design. Furthermore, we elucidated the molecular specificity of evolved variants by structural prediction and ligand docking in combination with experimental mutation scanning data. Finally, we expanded the biosensors' sensing range by integrating various enzyme modules capable of transforming non-native substrates into targets detectable by ligand-specific TFs. This modular approach allowed us to rapidly create highly orthogonal biosensors that can distinguish between IAA and its major precursors amid an environment of structurally similar analogs (Figure 1A).

RESULTS

The functional and structural analysis of IAA-responsive TrpR variants

The TrpR regulator, a well-documented transcription repressor, inhibits the transcription of TRP biosynthesis enzymes and its gene in the presence of sufficient TRP concentrations.[27] In its apo form, TrpR forms a symmetric homodimer, weakly binding to the *trp* operator via helix-turn-helix motifs (helix D-E)[28] (Figure S1). The binding of TRP enhances TrpR's affinity for the *trp* operator through alterations in the position of R84 guanidino-reading head and the addition of a hydrogen bond to DNA phosphate groups from its indole ring nitrogen.[28,29] Prior studies have explored TrpR's ligand preference toward a large variety of TRP metabolites, revealing a high degree of promiscuity for indole derivatives.[27,30,31]

Author Manuscript Author Manuscript Author Manuscript Author Manuscript

However, these studies primarily examined shifts in ligand-binding affinities of TrpR variants or differences in DNA-binding affinities caused by ligand variants. Consequently, existing structure-guided approaches to depict ligand specificity, particularly for dynamic regulation of TrpR variants at the transcription level, are limited.

Previous research has produced a variety of TrpR variants with unique DNA-binding capabilities, employing TRP as effectors by several directed evolution experiments.[32] Our investigation into the ligand specificity of these TrpR variants against a range of TRP derivatives revealed that those evolved variants are still promiscuous (Figures 1B, 1D, 2A, and S2). In general, α-substituted acids, such as 5-hydroxy-L-tryptophan (5HTP) and indole-3-pyruvic acid (IPyA), along with TRP, could enhance dimerization or DNA binding, subsequently repressing gene expression (Figures 2A and S2E). Conversely, smaller compounds without an amine group, including IPA, IAA, and IAld (also a precursor of indole-3-carboxylic acid), tended to disrupt the TrpR dimer or impede DNA binding, leading to gene derepression. Amines and amides such as TRM and indole-3-acetamide (IAM) exhibited variable effects on the DNA-binding ability of the TrpR homodimer, dependent on the structural variations of the mutants. These cross-activities hindered the use of TrpR in the engineering of IAA-producing enzymes for metabolic engineering or other applications, as IAA precursors could interfere with the signals produced by the IAA product itself. Therefore, we chose to further modify the $TrpR^{O1}$ system, which demonstrated the most significant fluorescence increase in response to IAA (Figures 1D, 2A, and S2E). This enhanced activation fold change was attributed to $TrpR^{O1}$'s superior repressive capabilities, offering the lowest basal-level fluorescence for dynamic range optimization (Figure S3A).

To determine the residues governing ligand specificity, we initially utilized the AlphaFold2 program to assess changes in the ligand-binding pockets (LBPs) of the $TrpR^{O1}$ variant caused by alterations in the DNA-binding region (helix D) (Figure S3B). The alignment of $TrpR^{O1}$ predicted structure, including its LBPs, closely matches that of the wild-type (WT) aporepressor (PDB: 3SSW) except for R84. This similarity allowed us to directly use the crystal structures of TrpR (PDB: 1TRO [TRP, DNA], 2OZ9 [TRP], and 6EJW [IAA]) for investigating the structure-function relationship. It is also important to note that the different orientation of R84 in the $TrpR^{O1}$ predicted structure compared to the $TrpR^{WT}$ aporepressor could play a significant role in influencing the intrinsic repression efficiency (Figures S3A and S3B).

The TrpR LBP consists of three key components. First, R84, positioned atop the binding pocket, acts as a pivotal control for DNA-binding affinity by interacting with the carboxyl group of TRP analogs. Second, the carbonyl backbone spanning residues 41–44 forms an electron-rich core, creating hydrogen bonds with the amino group or the indole N–H of TRP analogs. Lastly, R54 and E47 form a rigid foundation by a salt bridge that stabilizes the TrpR homodimer, providing π-cation interactions to accommodate indole derivatives (Figures 2B and S4). Previous studies have shown that α-substituted acids, such as TRP, and nonsubstituted acids, such as IAA, adopt two divergent binding poses within the receptor[30,31] (Figure 2B). Specifically, the amine group of α-substituted acids is anchored by the 41^{st} to 44^{th} residue backbone, along with an additional hydrogen bond from S88. In contrast, nonsubstituted acids primarily engage the same backbone to interact with the

Author Manuscript Author Manuscript Author Manuscript Author Manuscript

indole N–H group. The flip in binding orientation alters the spatial relationship between the R84 site and the 41–44 backbone, potentially affecting DNA-binding ability (Figure 2B).

To differentiate IAA from TRP binding, we initially targeted S88, following reports of its effectiveness in a fluorescence resonance energy transfer (FRET)-based biosensor via an S88Y mutation to eliminate TRP activity.[31] Nevertheless, this specific mutation did not yield the expected outcomes in our TF-based biosensor (Figure 2C). Instead, we discovered that substituting S88 with alanine (S88A) enhanced the IAA induction and reduced basal fluorescence probably through improved dimerization, attributed to alanine's smaller size and hydrophobic properties (Figures 2C and 2D).

The shrinkage of the binding pocket was also demonstrated through ligand-specificity analyses involving IPA, IAA, and IAld (Figures 2A and S3C). These three compounds, primarily differing in aliphatic chain length, serve as effective markers for assessing the size of the LBP (Figure 1A). Unlike the original $TrpR^{O1}$, the S88A variant preferentially accommodated the smallest IAld as the most potent derepressor, suggesting that substituting S88 into a smaller residue could result in a more compact binding pocket (Figures 2A and S3C). This observation was corroborated by an increase in basal fluorescence in the absence of ligand for mutations involving bulkier residues, indicating a destabilized TrpR aporepressor (Figure 2C). Notably, the S88 position did not directly participate in DNA binding, meaning that alterations here did not inherently affect DNA interactions. Furthermore, most variants retained their ability to repress expression in a TRP-dependent manner, implying that fluctuations in basal fluorescence were likely independent of intracellular TRP concentrations. Thus, beyond its role in hydrogen bonding, S88 modifications hypothetically influenced the size of LBP through adjustments in dimerization ability. While the S88A mutation successfully reduced affinity for most α-substituted TRP derivatives, additional engineering is required to comprehensively eliminate IPA and IAld binding (Figures 2F and S3C).

Manipulating TrpR dimerization interface to enhance IAA specificity

To refine the LBP size via TrpR dimerization efficiency, we targeted residues at the intersection of the dimerization interface and LBP, aiming for an optimal fit for medium-sized IAA. Building on the $TrpR^{O1}$ S88A mutant, we explored mutagenesis of M42, R48, T44, T81, and R84 (Figure 2B). Mutations at M42 and R48, either to smaller or hydrophobic residues, resulted in a more stable dimer, indicated by a reduced basal level of fluorescence, with IAld remaining the most effective derepressor (Figures 3A, S5A, and S5B). Mutations at T81 and R84 generally elevated basal fluorescence, suggesting a negative impact on TrpR aporepressor's DNA-binding capabilities (Figures S5C and S5D). Interestingly, selected variants at T81 or R84 also exhibited a shifted substrate preference toward IPA, suggesting an expanded LBP (Figure 3A). T44, positioned centrally among these residues, plays a crucial role in balancing dimerization and DNA-binding dynamics. Mutating T44 to smaller hydrophilic residues promoted repression presumably by increasing intrinsic DNA-binding ability, whereas larger sizes or shifts in hydrophobicity disfavored the process (Figure 2D).

Remarkably, we identified a variant exhibiting exclusive IAA activity through an additional T44M mutation (Figure 2D). This variant's ligand specificity for IAA was confirmed

Author Manuscript Author Manuscript Author Manuscript Author Manuscript

through transfer curves and an activity heatmap (Figures 2E and 2F). Furthermore, time-course fluorescence assays with varying concentrations of IAA, amid a mix of ten different TRP derivatives (each at 10 μM), revealed that the S88A + T44M mutations endowed the variant with resistance to analog interference, achieving detection limits as low as 50 μM (Figure 2G). Employing AlphaFold2 for structural prediction and RosettaLigand for flexible ligand docking,[33,34] we analyzed the mutant's ligand-receptor interactions (Figures 3C and S4). IAA adopted a pose in the LBP similar to its conformation within $TrpR^{WT}$, also displacing R84 outward from the LBP. Specifically, the S88A mutation reduced TRP-binding affinity, and the T44M mutation slightly expanded the LBP, decreasing its preference for IAld. Additionally, the substitution of T44 with the bulkier M44 residue effectively blocked binding with larger ligands due to steric hindrance, thereby enhancing ligand specificity (Figure 3C).

Utilizing the IAA-specific TrpR variant, we assessed the catalytic efficiency of the IAM hydrolase (IaaH) by monitoring the fluorescence response of the biosensor to IAA production (Figure S6A). The $TrpR^{O1}$ S88A + T44M double mutant, designed to be non-responsive to IAM, ensured that any observed fluorescence induction was solely attributable to increased IAA levels. Results demonstrated a significant, over 4-fold increase in fluorescence upon IaaH expression, directly correlating IaaH's catalytic activity with fluorescence intensity (Figure S6B). This configuration allows for the straightforward evaluation of IaaH functionality via the IAA biosensor, free from substrate IAM interference. Nevertheless, IaaH's capability to also facilitate the conversion of IPyA into IAA posed a challenge for achieving absolute molecular specificity, indicating the necessity for further engineering to address its promiscuity (Figures S6A and S6C).

Decoupling TRP repression ability in the mixture of TRP and IAA

In experiments where TRP and IAA were mixed in a 1:1 ratio, the double mutants still exhibited TRP-dependent activity patterns (Figures 2D, 3F, and S5). To completely decouple the TRP repression during IAA activation, it is crucial to eliminate all possible binding sites for TRP. Previous mutagenesis at R84 produced a variant, R84A, which interestingly showed TRP activity mirroring that of IAA, characterized by gene activation rather than repression (Figures 3A and S7A). This shift suggested that TRP adopted a binding pose resembling that of IAA. Additionally, the observed IPA dominance for S88A + R84 mutants suggested an enlargement of the LBP (Figure 3A), which allowed those variants to accommodate TRP in a pose similar to IPA. To restore the ligand preference for IAA, we combined mutations at M42, T44, or M48 with S88A + R84A, aiming to further tighten the TrpR dimer (Figure S8).

Subsequent saturation mutagenesis efforts identified several triple mutants that predominantly favored IAA activity, exhibiting minimal TRP repression even when exposed to equal concentrations of TRP and IAA (Figures 3B and S8). Mutating M42 to smaller hydrophilic residues such as N or Q, or to hydrophobic residues such as V or Y, perhaps facilitated tighter dimer formation, effectively narrowing the LBP to exclude TRP binding (Figures 3B and S8A). In addition, substituting R48 with hydrophobic residues exhibited similar ligand preference (Figures S8C and S8D). Among these, the S88A + R84A +

Author Manuscript Author Manuscript Author Manuscript Author Manuscript

M42V triple mutation emerged as particularly IAA selective, abolishing TRP binding while maintaining IAA-dominating induction under varying conditions of TRP and IAA exposure, as demonstrated through transfer curves and ligand-specificity analysis (Figures 3B, 3D, 3F, and S7B). This novel biosensor could enable the accurate assessment of multi-step IAA synthesis from TRP, overcoming intermediate interference and TRP repression—a limitation unaddressed by previous biosensors that retained R84 as a regulatory latch.

Structural predictions and ligand-docking simulation revealed a profound transformation in IAA's binding conformation within this variant, where IAA adopted an unconventional pose. Specifically, the benzene segment of IAA's indole backbone protruded from the binding pocket (Figure 3E). Without R84, IAA's carboxyl group engaged in an alternative interaction with T81, akin to IPA,[30] causing the indole backbone to lean outward from the binding pocket. This shift could also account for the observed elimination in IAA activity with T44 mutations in the $TrpR^{O1}$ S88A + R84A context, as larger substitutions would clash with the indole structure (Figure S8B). Additionally, in the absence of R84, IAA's carboxylate would interact with R54—a key dimer stabilization contributor through its interaction with the coplanar E47 (Figures 3E and S4). Consequently, IAA binding would possibly alter the planar hydrogen bond between R54 and E47, diminishing its dimerization affinity (Figure 3E).

The functional and structural analysis of TynA and FeaR variants

In our previous work, we demonstrated that the FeaR sensor could detect various aromatic aldehydes produced from neuroactive amines by the promiscuous monoamine oxidase TynA[21] (Figure S9A). Among these amines, TRM also acts as a precursor of IAA through subsequent oxidation of IAAld (Figure 1A). Expanding on the prior research, we characterized the ligand promiscuity of the TynA-FeaR sensor system in EcN utilizing orthologs from *Klebsiella* species, *Klebsiella pneumoniae* and *Klebsiella aerogenes* (Figures 4A and S10). TynA from *K. pneumoniae* ($TynA^{KP}$) was successfully expressed in *E. coli* fused with an *E. coli* TynA ($TynA^{MG}$) signal peptide, whereas TynA from *K. aerogenes* ($TynA^{KA}$) exerted a significant growth defect on EcN. $TynA^{KP}$ also showed diminished activity in EcN, active only in its soluble form, unlike the robust activity seen in both soluble and membrane-bound forms of $TynA^{MG}$ (Figure S9B). Moreover, $TynA^{KP}$ was inactive in the absence of $TynA^{MG}$'s signal peptide, demonstrating the vital role of the signal peptide in enhancing enzyme solubility. Despite literature suggesting the superior activity of *Klebsiella* TynA for dopamine (DA),[35] our findings revealed similar substrate promiscuity between $TynA^{MG}$ and $TynA^{KP}$ when expressed in EcN (Figure S9B and Table S1).

However, exploring various TynA and FeaR combinations revealed ligand-specificity shifts attributable to FeaR variations, likely due to lower sequence identities (Figures 4A and S9C). It also supported our previous findings that biosensing specificity is more effectively modulated by regulator mutations than by enzymatic modifications.[21] Coupling with *K. pneumoniae* FeaR ($FeaR^{KP}$) drastically reduced all activities, regardless of the choice of the starting codon or the source of TynA (Figure S9C). However, pairing with *K. aerogenes* FeaR ($FeaR^{KA}$) significantly enhanced the response to TRM, matching the levels seen with tyramine (TYM) or phenylethylamine (PEA) (Figures 1D and 4A).

Author Manuscript Author Manuscript Author Manuscript Author Manuscript

E. coli and *K. aerogenes* FeaR showed conservation in the ligand-binding sites, with only six mutations within the LBP (Figure 4B). Those mutations slightly increased overall hydrophobicity, which illustrated the observed attenuated DA activity in $FeaR^{KA}$ (Figures 4A and S11A). Subsequent structural analysis revealed $FeaR^{KA}$'s enhanced TRM binding and activity were due to an additional hydrogen bond with Q117 (Figures 4B and S12). Notably, I109 and I84 (corresponding to L100 and M83 in $FeaR^{MG}$) were vital for the unique ligand-binding conformation in $FeaR^{KP}$, with significant side-chain rotations relative to $FeaR^{MG}$ (Figure 4B). M83 emerged as key in regulating hydroxyl group interactions with TYM or DA aldehyde in $FeaR^{MG}$, and L108 engaged in universal π-alkyl interactions with aromatic rings.[21] In $FeaR^{KA}$, the slightly bulkier base of I109's s-butyl group inhibited W111 from forming π interactions with IAAld, and its slimmer side-chain head better accommodated the large indole ring of IAAld. Meanwhile, the more rigid I84 in $FeaR^{KA}$, compared to the flexible M83 in $FeaR^{MG}$, restricted IAAld's indole backbone from deeper insertion into the binding pocket. These alterations supported indole N–H hydrogen bonding with Q117, diverging from *E. coli* FeaR where W110's π interactions were dominant. Consequently, we preserved the I84 mutation to maintain hydrogen bonding with Q117 and initiated mutagenesis at I109, given its strategic position for refining TRM specificity (Figure 4B).

Optimizing ligand specificity and activity for TRM sensors

We randomized the I109 residue for $FeaR^{KA}$ and evaluated the activity of all 19 variants, coupled with $TynA^{KP}$, against five structurally similar amines (Figure 4C). $TynA^{KP}$ was employed because it showed better compatibility with $FeaR^{KP}$, which shared 80% sequence identity with $FeaR^{KA}$ (Figures S9C and S10). This approach yielded several ligand-specific variants with exclusive responses to the three predominant ligands: I109F for phenylacetaldehyde (PEAld), I109T and I109N for IAAld, and I109E specifically for 4-hydroxyphenylacetaldehyde (TYM aldehyde) (Figure 4C).

These findings highlighted I109 as a critical determinant of ligand specificity through steric effects or polar interactions caused by mutations. Increasing the size of residue from I to F could eliminate activities for ligands larger than PEA. Additionally, replacing I109 with the negatively charged E reduced affinity for hydrophobic moieties such as PEA's benzene and TRM's indole structure, preserving only TYM activity.

Altering I109 to smaller hydrophilic residues such as T or N selectively removed PEA and TRM activities, rendering IAAld as the sole bound ligand. The I109L mutation diminished TRM activity while a smaller but structurally similar I109V mutation enhanced TRM activity, illustrating the importance of I109 in $FeaR^{KA}$ for optimal interaction with IAAld compared to $FeaR^{MG}$. Notably, the structural analysis revealed that I84 remained a rigid support for IAAld's indole backbone, and N109 exhibited a larger bond-rotation angle relative to L108 in the $FeaR^{MG}$ than that of I109 (Figures 4B, 5B, and S12). Mutating I109 to N likely generated greater repulsion to the W111, thus diminishing its interaction with all other ligands while allowing more space for IAAld. Finally, the I-to-N mutation could form a π-donor hydrogen bond particularly with IAAld's indole group, conferring I109N as the best IAAld-specific variant (Figure S12).

Author Manuscript Author Manuscript Author Manuscript Author Manuscript

To improve the fluorescence output of the TRM-specific sensor consisting of $TynA^{KP}$ and $FeaR^{KA}$ I109N, we supplemented M9 medium with 1 mM thiamine and 0.2% trace elements to enhance cell growth and signal amplification (Figures S11B and S13A). Additionally, we relocated the FeaR regulator cassette to the reporter plasmid with a slightly higher copy number, boosting the gene activation (Figures 5A and S11B). Although we considered augmenting TynA's activity to facilitate aldehyde formation from amines, rapid conversion of PEA by TynA led to minor cross-activity in the $FeaR^{KA}$ I109N variant (Figures S11B and S13B). Hence, we continued utilizing $TynA^{KP}$ to maintain signal orthogonality. These optimizations resulted in a more than 1,000-fold increase in fluorescence response to TRM while constantly surpassing the response to other amines, which induced less than a 10-fold increase (Figures 5C and S11B).

Similar to the IAA-specific sensor, we tested the sensor's sensitivity through a kinetic fluorescence assay against increasing TRM concentrations, with and without a background of ten different TRP analogs (each at 10 μM) (Figures 5D and S13B). The sensor demonstrated a stable, dose-dependent response to TRM, maintaining accuracy in the presence of interfering substances. This TRM-specific biosensor exhibited high sensitivity, detecting as low as 10 μM TRM, with a rapid response observed within 1 h of ligand introduction. Additionally, the consistent baseline in the absence of TRM underscored the sensor's high signal-to-noise ratio for potential applications (Figure 5D).

Expanding the FeaR biosensing range by a plug-and-play strategy

Apart from the IAM and TRM pathways, the IPyA pathway is recognized as the most predominant and widespread pathway for IAA synthesis in bacteria.[36] This three-step process first converts TRP to IPyA by an amino acid aminotransferase (AAT). Next, IPyA is catalyzed into IAAld via the action of indole pyruvate decarboxylase (IpdC). Finally, an aldehyde dehydrogenase oxidizes IAAld, a step also shared with the TRM pathway (Figure 1A). Additionally, IPyA serves as a precursor to IPA production, through intermediates, including indole-3-lactic acid and indole acrylic acid.[7] While these downstream IPyA metabolites perform diverse roles within the human gut, the psychological effects of IPyA itself remain unclear. Developing an IPyA sensor could thus aid in understanding IPyA's significance and guide the engineering of enzymes involved in its metabolism.

Expanding on our established ligand-specific TynA-FeaR sensors, we introduced the IpdC enzyme to convert aromatic pyruvates into aldehydes detectable by FeaR (Figures 1C and 6A). Contrary to anticipated specificity, IpdC demonstrated a high degree of enzyme promiscuity, catalyzing reactions beyond IPyA (Figures 1D and S14). Due to the native aromatic pyruvate biosynthesis in EcN,[37,38] constantly produced substrates led to an elevated basal fluorescence compared to the TynA-FeaR system with the same configuration. Moreover, the IpdC-FeaR system also exhibited a lower dynamic range and a higher half-maximal effective concentration than the TynA-FeaR system (Figures 1D and S14A). These observations emphasize the need for additional modifications to IpdC's catalytic efficiency and specificity to enable its further application in biosensing and biomanufacturing.

Author Manuscript Author Manuscript Author Manuscript Author Manuscript

Given IpdC's innate substrate preference for phenylpyruvic acid (PPyA) over IPyA, we decided to first construct a PPyA sensor without substantial modifications to the enzyme module. Previously, we identified $FeaR^{WT}$ A81L as a biosensor specifically responsive to PEAld, so we replaced the promiscuous FeaR with the A81L variant aiming for PPyA-specific biosensing (Figures 6B and 6C). Similar to the TRM-specific sensor, we integrated the FeaR A81L regulator on the reporter plasmid to amplify the signal (Figure 6A). To minimize any potential growth impact, we kept the weak ribosome-binding site (RBS) used for *tynA* to express IpdC, enabling the rapid construction of a PPyA-specific biosensor. This sensor retained high specificity, showing stable dose-dependent fluorescence with minimal noise signals caused by the addition of interfering molecules, although its detection threshold exceeded 100 μM (Figures 6C and 6E).

When directly coupled with the IAAld-specific FeaR module previously characterized, the IpdC cassette produced extremely low signals, and signals from PPyA remained prominent (Figure S14). Due to the lower detection sensitivity compared with the TynA-FeaR system, we optimized the expression of IpdC for the better conversion of IPyA to IAAld. This would enhance the specific detection of IPyA, a less favored substrate. However, higher levels of IpdC expression caused growth defects in EcN, suggesting that aldehyde product accumulation from continuous IpdC activity on intracellular aromatic pyruvates might be toxic. To circumvent this, we fused a signal peptide from $TynA^{WT}$ to IpdC, directing the aldehydes to the periplasm, and created an RBS library to fine-tune expression levels (Figure 6B). Screening this library led to the identification of an IPyA-specific variant, whose activity toward PPyA was effectively restrained by the FeaR I109N mutant (Figure 6D). Ligand-specificity analysis revealed that this sensor was dedicated to IPyA aside from the two precursors, TRP and IPA (Figures 6E and S15). TRP could be converted to IPyA through an EcN endogenous AAT pathway, and we hypothesized that IPA could be converted to IPyA through reversible enzyme cascades under rapid IPyA consumption conditions.[7,38] The sensor's time-course fluorescence assays demonstrated consistent responses to IPyA concentrations, unaffected by the presence of a mixture of interfering substances (Figure 6D). In the future, this biosensor holds promise for biosensor-aided enzyme engineering to enhance microbial IAA production via the IPyA pathway.

DISCUSSION

Signal orthogonality is fundamental for all chemical sensors, yet achieving it poses a challenge for biosensors due to the inherent promiscuity of biological regulatory elements.[39] This is particularly evident in TrpR and FeaR, which, contrary to initial expectations, have demonstrated notable promiscuity in our extensive examinations of their substrate scopes. Here, we established a generalizable approach to engineer the molecular specificity of these transcriptional biosensors for accurately detecting a range of gut-microbiota-derived TRP metabolites.

To initiate the evolution process, we first systematically examined the natural or synthetic orthologs for these two TFs, TrpR and FeaR, analyzing sequence and structural variations to unveil their distinct substrate preferences. To understand the sequence-structure-function relationships and ligand-specificity transition over the evolution processes, we

Author Manuscript Author Manuscript Author Manuscript Author Manuscript

established a structural prediction pipeline using models, including AlphaFold2[33,40,41] and RosettaLigand,[34,42,43] which could rapidly generate ligand-docking simulations for proteins not yet characterized. It is important to note that while these models can predict various conformations, the highest-ranked conformation—considered most favorable based on the lowest calculated free energy—sometimes failed to align with empirical data. Consequently, we relied heavily on existing experimental results and findings from our current study to identify the most accurate conformation that aligns with experimental evidence. Additionally, traditional saturation mutagenesis proved invaluable, often revealing insights beyond our initial expectations and elucidating the sequence-function relationship of residues crucial for specificity control.

Selecting a variant exhibiting the highest fold change for our target ligand as the starting point for protein evolution, we harnessed structural insights alongside experimental data to steer subsequent evolution processes targeting IAA and IAAld. Specifically, in TrpR, where LBP is formed by two chains in the homodimer, we managed to reduce promiscuous binding by disrupting the unique S88 hydrogen bond associated with TRP. Innovatively, we employed IPA, IAA, and IAld as indicators of LBP size, reasoning that a preference for smaller ligands implies a more compact dimer. We first reported a novel S88A mutation for enhanced repression on Ptrp, thus resulting in a greater fold change for IAA and, unexpectedly, for IAld as well. We then fine-tuned the size of LBP to avoid strengthening interactions with the smaller ligand IAld by an additional mutation at T44M while still excluding large molecules such as TRP, IPyA, or IPA. During the evolution process, we targeted residues at the dimerization interface within the ligand-binding domain. Mutations at T81 and R84 successfully expanded the LBP probably by weakening dimerization, with IPA emerging as the primary effector. Conversely, mutations at M42 and R48 effectively narrowed the LBP presumably by reinforcing the TrpR dimer, with IAld as the dominant effector. These modifications provide a programmable framework for the LBP, opening avenues for further development of IPA- or IAld-specific sensors. Finally, we integrated the IAA-specific regulator, $TrpR^{O1}$ S88A + T44M, with the IaaH enzyme module, demonstrating the sensor's efficacy in detecting intracellular IAA produced via enzymatic reaction. This proof-of-concept demonstration highlights the potential of the IAA-specific sensor for aiding in enzyme evolution and metabolic engineering.

We also discovered that TRP-nonresponsive TrpR variants, when exposed to both TRP and IAA simultaneously, exhibited fluorescence patterns akin to those observed under "TRP-only" conditions. This suggests that the aporepressor may still favor TRP binding, although TRP does not function as an effector to alter TrpR's DNA-binding affinity significantly. This previously unreported phenomenon underscores a novel area of TrpR functionality that required resolution. To address the potential of TRP binding that facilitates the dimerization of the TrpR aporepressor, we employed an S88A + R84A double mutation to obliterate another TRP-binding site. As a result, TRP binding shifted from stabilizing the aporepressor to acting as a derepressor, similar to the roles of IPA or IAA. Initiating from this mutated version, we undertook further modifications to adjust the LBP's size, successfully reinstating IAA as the predominant effector for selective biosensing. Although the ~3-fold fluorescence induction observed with this novel biosensor is relatively modest, it offers unprecedented potential for assisting in *de novo* IAA biosynthesis from TRP. This

Author Manuscript Author Manuscript Author Manuscript Author Manuscript

capability is particularly noteworthy, as no prior transcriptional biosensor could selectively respond to IAA amid high TRP concentrations, marking a significant leap forward in biosensor design and application.

In the case of the FeaR regulator, where the LBP is situated within a monomer, we applied canonical engineering principles distinct from those used for TrpR.[21,22] For monomers, a larger residue introduces a greater steric effect, consequently constricting the LBP. On the other hand, a smaller residue provides additional space, accommodating bulkier ligands but potentially compromising interactions with smaller residues. Our investigation into FeaR homologs from *Klebsiella* species emphasized the value of experimental analysis for understanding ligand specificity, revealing $FeaR^{KA}$'s exceptional affinity for TRM. By comparing the predicted structure of $FeaR^{KA}$ with the *E. coli* version, I109 emerged as a key determinant of ligand preference. We demonstrated how targeted mutagenesis could significantly alter ligand specificity, converting a promiscuous regulator into ones selectively responsive to IAAld, PEAld, or 4-hydroxyphenylacetaldehyde.

Given the limited solubility and stability of these aldehyde compounds for direct dosing,[44] we utilized the TynA enzyme module to transform aromatic amines into the corresponding aldehydes. This approach led to the identification of the first IAAld-specific TF, $FeaR^{KA}$ I109N, and a TRM-specific sensor when combined with TynA. Furthermore, we refined the sensor's configuration to enhance signal dynamic range, resulting in a TRM-specific sensor characterized by a low detection limit and minimal cross-reactivity. Building on the previously identified PEAld-specific FeaR A81L, we expanded our biosensor repository by integrating the FeaR regulator with a different converting enzyme, IpdC. This modular approach allowed us to rapidly generate a new PPyA-specific sensor. By tailoring IpdC's expression, we also crafted an IPyA-specific sensor that exhibits high selectivity, effectively distinguishing IPyA from structurally similar compounds. However, the presence of the native AAT pathway, which converts TRP to IPyA, alongside hidden routes that convert IPA into IAAld, made the sensor not solely responsive for IPyA. To better achieve the desired molecular specificity within this EcN biosensor framework, we could knock out the enzymes in these IPyA-producing pathways for future applications.

Collectively, this work demonstrates the power of structure-guided protein engineering to create highly specific transcriptional biosensors, overcoming the inherent promiscuity that often limits the direct use of natural receptors. Through a combination of evolutionary analysis, structure-guided mutagenesis, and the integration of modular enzymes, we successfully developed a collection of biosensors capable of selectively detecting IAA, IAM, TRM, IPyA, PEA, and PPyA amid a complex matrix of structurally similar compounds. The resulting biosensing platform provides a versatile toolbox for precisely quantifying key gut microbiota metabolites, enabling applications ranging from diagnostics and therapeutics to metabolic engineering.[6,45] Additionally, given the important roles of those compounds in plant-microbe interactions, the developed biosensors will be useful in elucidating the soil ecosystem's dynamic interactions and engineering the plant-microbe community for practical applications.[46–48] Future efforts to expand the detection repertoire and improve the sensors' performance characteristics will likely yield valuable further insights into the complex roles of TRP derivatives in human health and disease.[2,49]

Author Manuscript Author Manuscript Author Manuscript Author Manuscript

EXPERIMENTAL PROCEDURES

Plasmids, strains, and reagents

All strains, plasmids, and sequences of genetic parts used in this study are summarized in Tables S2–S4, respectively. *E. coli* DH10B (Invitrogen, Waltham, MA, USA) was used for all routine cloning and mutagenesis plasmids assembled by Gibson Assembly or Golden Gate Assembly methods. All biosensor systems were characterized in *E. coli* Nissle 1917 (DSMZ, Germany). The *tynA*, *feaR*, and *trpR* genes were obtained from *E. coli* MG1655 genomic DNA. The *tynA* and *feaR* genes from *Klebsiella* species were synthesized by Twist Bioscience (San Francisco, CA, USA). The *ipdC* from *Enterobacter cloacae* was synthesized by Integrated DNA Technologies (Coralville, IA, USA). The *gfpmut3* sequence was fused with an SsrA degradation tag to report changes in outputs over time. Primers were purchased from Integrated DNA Technologies. Plasmid DNA was purified using the PureLink Quick Plasmid Miniprep Kit (Invitrogen), and PCR products were extracted from electrophoresis gels using the Zymoclean Gel DNA Recovery Kit (ZYMO Research, Irvine, CA, USA). Enzymes were purchased from New England Biolabs (Ipswich, MA, USA). Chemicals were purchased from Sigma-Aldrich (St. Louis, MO, USA). Antibiotics were purchased from Gold Biotechnology (Olivette, MO, USA). LB Miller (LB) medium (VWR, Radnor, PA, USA) was used for routine cloning, enzymatic assays, and seed culture of fluorescence assays. LB with 1.5% agar was used for the transformation of *E. coli* DH10B and Nissle 1917. M9 minimal medium supplemented with 2 mM $MgSO_4$, 100 μM $CaCl_2$, 0.4% (w/v) glucose, 0.2% casamino acids, and 0.01% thiamine was used for TrpR-Ptrp sensor assays. M9 minimal medium supplemented with 2 mM $MgSO_4$, 100 μM $CaCl_2$, and 2% (w/v) glycerol was used for TynA-FeaR-PtynA sensor assays unless otherwise indicated. M9 minimal medium supplemented with 2 mM $MgSO_4$, 100 μM $CaCl_2$, 2% (w/v) glycerol, 1 mM thiamine, and 0.2% trace element mix was used for IpdC-FeaR-PtynA sensor assays. Interfering ligand stock was prepared by dissolving 1 mM 5HTP, TRP, IPA, IPyA, IAA, IAM, indole-3-carboxaldehyde (IAld), 5HT, tryptamine (TRM), dopamine (DA), tyramine (TYM), PEA, and PPyA in 50% ethanol and diluted 100× into experimental cultures.

Gene knockout

Gene knockout was performed following the previous report.[50] To construct an EcN variant with genomic *trpR* knocked out, pMYF42 was obtained by inserting the gRNA derived from the *trpR* sequence and the template with 500-bp homologous arms flanking the *trpR* loci into pgRNA. EcN was transformed with pMP11 and grown on LB plates with 100 μg/mL ampicillin at 30°C overnight. 5 mL of LB with 100 μg/mL ampicillin was inoculated with a single colony and grown overnight at 250 rpm and 30°C. The overnight culture was diluted 50-fold into 25 mL of LB with 100 μg/mL ampicillin and 1% arabinose (to induce recombinase expression) in a 250-mL shake flask and grown at 250 rpm and 30°C until optical density (OD_{600}) was 0.35–0.4. The cells were harvested and prepared for transformation via electroporation. Competent cells were transformed with 300 ng of pMYF42 and recovered in 600 μL of SOC medium for 2 h at 250 rpm and 30°C. Following recovery, cells were plated on LB with 100 μg/mL ampicillin and 34 μg/mL chlorophenol plates and grown overnight at 30°C. Gene knockout was confirmed by colony PCR. For plasmid curing, pMYF42 was cured by growing the single colony in 5 mL of LB with 100

Author Manuscript Author Manuscript Author Manuscript Author Manuscript

μg/mL ampicillin and 200 ng/mL anhydrotetracycline (aTc) at 250 rpm and 30°C to induce the expression of a gRNA targeting the pBR322 origin. That culture was then plated onto LB plates with no antibiotic and grown at 42°C to cure out pMP11.

TrpR-Ptrp fluorescence assays

Single colonies of EcN-*Δtrp* harboring the respective sensor and reporter plasmids were inoculated into 5 mL of LB medium and incubated overnight at 37°C with shaking at 250 rpm. Experimental cultures were prepared by diluting overnight cultures 200× into 0.6 mL of fresh M9 medium supplemented with respective ligands in 2-mL 96-deep-well plates. Cultures were grown for 8 h at 37°C and 250 rpm before collecting samples for flow-cytometry analysis. For IaaH-TrpR-based sensor systems, cultures were grown for 24 h under the same condition before flow-cytometry analysis. All media were supplemented with the relevant antibiotics for plasmid maintenance (34 μg/mL chloramphenicol and 100 μg/mL spectinomycin).

Time-course TrpR-Ptrp fluorescence assays

Single colonies of EcN-*Δtrp* harboring the respective sensor and reporter plasmids were inoculated into 5 mL of LB medium and incubated overnight at 37°C with shaking at 250 rpm. Experimental cultures were prepared by diluting overnight cultures 200× into 0.6 mL of fresh M9 medium in 2-mL 96-deep-well plates. After 2 h, cultures were supplemented with varying concentrations of IAA, with or without interfering ligands. Cultures were grown for 8 h at 37°C and 250 rpm, and samples were collected every 1 h for flow-cytometry analysis. All media were supplemented with the relevant antibiotics for plasmid maintenance (34 μg/mL chloramphenicol and 100 μg/mL spectinomycin).

High-performance liquid chromatography

The compositions of products resulting from IaaH enzyme activity on IAM, IAA, IAld, IPA, and IPyA were analyzed by HPLC using an Agilent 1260 Infinity II HPLC system equipped with a Poroshell 120 EC-C18 column (4.6 mm × 100 mm, 2.7 mm particle size) and a UV detector set at 280 nm (Agilent Technologies, Santa Clara, CA, USA). Three independent replicates were taken from both the initial medium and the supernatant after a 24-h enzymatic reaction by EcN expressing the IaaH enzyme. The mobile phase contains water (0.1% formic acid) and acetonitrile (0.1% formic acid). For the elution, a gradient of water and acetonitrile, both containing 0.1% formic acid, was used. The gradient started at 92% water and 8% acetonitrile, shifted to 74/26 at 5 min, balanced to 50/50 at 8 min, and returned to 92/8 at 10 min. The column was maintained at a temperature of 60°C with a flow rate of 1 mL/min.

FeaR-PtynA fluorescence assays

Single colonies of EcN harboring the respective sensor and reporter plasmids were inoculated into 0.6 mL of LB medium and incubated overnight at 37°C with shaking at 250 rpm. Experimental cultures were prepared by diluting overnight cultures 100× into 0.6 mL of fresh M9 medium in 2-mL 96-deep-well plates. After 2 h, cultures were supplemented with varying concentrations of respective ligands in 2-mL 96-deep-well plates. Cultures

Author Manuscript Author Manuscript Author Manuscript Author Manuscript

were grown for 24 h at 37°C and 250 rpm before collection of samples for flow-cytometry analysis. All media were supplemented with the relevant antibiotics for plasmid maintenance (20 μg/mL kanamycin and 100 μg/mL spectinomycin).

Time-course kinetic fluorescence assays

Single colonies of EcN harboring corresponding sensor and reporter plasmids were inoculated into 0.6 mL of LB medium and incubated overnight at 37°C with shaking at 250 rpm. Experimental cultures were prepared by diluting overnight cultures 100× into 0.6 mL of fresh M9 medium in 2-mL 96-deep-well plates. After 2 h of incubation at 250 rpm and 37°C, cultures were supplemented with varying concentrations of respective ligands with or without interfering ligands and transferred to 96-well assay microplates. The fluorescence and culture absorbance (Abs) were recorded every 15 min within a Tecan Infinite M200 Pro plate reader (Tecan, Switzerland) for 10 h of incubation at 200 rpm and 37°C. Baseline fluorescence and Abs recorded from the medium alone were subtracted from the values of each test sample. The corrected fluorescence was then normalized by dividing by the Abs and further corrected by subtracting the value obtained from non-fluorescent WT cells, as outlined in Equation 1. All media were supplemented with the relevant antibiotics for plasmid maintenance (20 μg/mL kanamycin and 100 μg/mL spectinomycin).

$$\text{Fluorescence(a.u.)} = \frac{\text{Fluorescence}_{\text{sample}}}{\text{Abs(600nm)}_{\text{sample}}} - \frac{\text{Fluorescence}_{\text{wild-type}}}{\text{Abs(600nm)}_{\text{wild-type}}}. \quad \text{(Equation 1)}$$

Flow cytometry

Cultures were diluted to 200 μL in filter-sterilized PBS supplemented with 2 mg/mL kanamycin and transferred to 96-well U-bottom assay microplates (BD Biosciences, San Jose, CA, USA). The fluorescence of individual samples, with an OD_{600} of approximately 0.005–0.01, was measured using a Millipore Guava EasyCyte High Throughput flow cytometer equipped with a 488-nm excitation laser and a 512/18-nm emission filter (MilliporeSigma, Burlington, MA, USA). Data from cytometry were gated based on forward and side scatter and subsequently analyzed using FlowJo software (FlowJo, Ashland, OR, USA). Arithmetic means from three independent biological experiments were calculated and averaged. Baseline fluorescence, recorded from non-fluorescent WT cells, was subtracted from the fluorescence of each test sample, according to Equation 2. The normalized activity of each specific sensor system for TRP analogs relative to the targeted ligand was calculated according to Equation 3.

$$\text{Fluorescence(a.u.)} = \text{Fluorescence}_{\text{sample}} - \text{Fluorescence}_{\text{wild-type}}, \quad \text{(Equation 2)}$$

$$\text{Normalized activity} = \frac{\text{Fluorescence}_{\text{Ligand}} - \text{Fluorescence}_{\text{none}}}{\text{Fluorescence}_{\text{Targeted ligand}} - \text{Fluorescence}_{\text{none}}}.$$

Author Manuscript Author Manuscript Author Manuscript Author Manuscript

(Equation 3)

Hill equation fitting

The Hill equation was employed to model the response curves of the fluorescence data using Equations 4, 5, and 6 to establish the relationship between ligand concentration and fluorescence response. The root-mean-square error (RMSE) was calculated using Equation 7 and minimized by the solver tool in Excel to fit the experimental data. Fitted values are listed in Table S5.

For repressible constructs

$$F = F_{\max} - \frac{(F_{\max} - F_{\min})}{(K_A/[L])^n + 1},$$

(Equation 4)

for inducible constructs

$$F = F_{\min} - \frac{(F_{\max} - F_{\min})}{(K_A/[L])^n + 1},$$

(Equation 5)

and for inducible constructs with substrate inhibition

$$F = F_{\min} + \frac{(F_{\max} - F_{\min})}{(K_A/[L])^n + 1 + ([L]/K_i)^{n_i}},$$

(Equation 6)

where F is calculated fluorescence, $F_{\max}$ is maximum fluorescence, $F_{\min}$ is minimum fluorescence, K_A is half-maximal constant, K_i is half-maximal inhibition constant, n and n_i are Hill coefficient and inhibition coefficient, respectively, and $[L]$ is ligand concentration.

$$\mathrm{RMSE} = \sqrt{\sum_{N=1}^{N} (F - F_{\exp})^2 / N},$$

(Equation 7)

where F is calculated fluorescence, $F_{\exp}$ is actual experimental fluorescence, and N is number of data points.

Enzymatic assays

The activity of TynA was evaluated using a colorimetric assay to measure the rate of hydrogen peroxide (H_2O_2) production, adapting from previous literature.[51] H_2O_2, a by-product of the TynA reaction as described in Equation 8, was quantified by the Amplex Red Hydrogen Peroxide Assay Kit (Invitrogen). Single colonies of EcN harboring TynA sourced from *E. coli* MG1655 ($TynA^{MG}$), from *K. pneumoniae* ($TynA^{KP}$), and $TynA^{KP}$

Author Manuscript Author Manuscript Author Manuscript Author Manuscript

fused with the TynA^{MG} signal peptide (TynA^{KP} + SP^{MG}) were respectively inoculated into 5 mL of LB medium and incubated overnight at 37°C with shaking at 250 rpm. Overnight cultures were diluted 100× into 50 mL of fresh LB medium in baffled Erlenmeyer flasks and incubated at 250 rpm and 37°C for 2 h. 100 ng/mL aTc was added to induce the expression of TynA enzymes and incubated at 250 rpm and 37°C for 12 h. Cells equivalent to a total OD_{600} of 30 were harvested, washed three times with PBS, and resuspended in 3 mL of lysis buffer containing 1 mg/mL lysozyme and 1 mM phenylmethylsulfonyl fluoride. The cells were lysed via sonication on ice for 5 min. The crude protein in the cell debris and lysate supernatant was collected by centrifugation at 10,000 × *g* for 1 h. The cell debris was then resuspended in a volume of lysis buffer equal to that of the cell lysate. 45 μL of crude protein extract was mixed with 5 μL of 2 mM ligands and incubated at 37°C for 15 min. 50 μL of Amplex Red reagent working solution was added to each sample, along with standards containing known concentrations of H_2O_2 to establish a standard curve. After 1 h of incubation at room temperature, the H_2O_2 concentration of each sample was determined according to the H_2O_2 standard curve using the Tecan microplate reader (Infinite M200 Pro) with excitation at 545 nm and emission at 590 nm. Baseline fluorescence, recorded from WT cells, was subtracted from the fluorescence of each test sample, according to Equation 2. All growth medium was supplemented with the relevant antibiotics for plasmid maintenance (100 μg/mL ampicillin).

$$R-CH_2NH_2 + H_2O + O_2 \xrightarrow{TynA} R-CHO + H_2O_2 + NH_3 . \quad \text{(Equation 8)}$$

Molecular modeling

FeaR monomers, FeaR dimers, and TrpR dimers with targeted mutations were modeled using ColabFold v1.5.5, utilizing AlphaFold2 or AlphaFold2_multimer_v3 as the prediction models. One of the five top-ranked predictions was relaxed using Amber and used as a receptor for ligand docking. Ligand-binding sites were identified using the DeepSite program[52] (https://playmolecule.org/deepsite/), and the plausible locations of LBPs were documented as starting coordinates for ligand docking. Ligand-docking simulations were conducted with the RosettaLigand program, hosted by the ROSIE webserver (https://rosie.rosettacommons.org/). Ligand conformers generated by BCL were uploaded to the ROSIE webserver along with the protein structure PDB file.[53] 2D diagrams of protein-ligand interactions were created using Discovery Studio v21.1.0 (BIOVIA, San Diego, CA, USA), and 3D protein structures were visualized with ChimeraX v1.7.1 (UCSF, San Francisco, CA, USA).

RESOURCE AVAILABILITY

Lead contact

Further information and requests for resources should be directed to and will be fulfilled by the lead contact, Tae Seok Moon (tsmoon7@gmail.com).

Author Manuscript Author Manuscript Author Manuscript Author Manuscript

Materials availability

The study did not generate unique materials.

Supplementary Material

Refer to Web version on PubMed Central for supplementary material.

ACKNOWLEDGMENTS

We thank Matthew Lima for helping with experiments and Sandra Matteucci and Allison Creighton for helping to revise the manuscript. This work was supported by the National Science Foundation (MCB-2001743 to T.S.M.), National Institutes of Health (RO1 AT009741 to T.S.M.), the United States Department of Agriculture (2020-33522032319 to T.S.M.), and the US Environmental Protection Agency (84020501 to T.S.M.). The content is solely the responsibility of the authors and does not necessarily represent the official views of the funding agencies.

Data and code availability

The data that support the findings of this study are provided in the main text, supplemental information, or Data S1. All other relevant data are available from the lead contact upon reasonable request.

REFERENCES

1. McCann JR, and Rawls JF (2023). Essential Amino Acid Metabolites as Chemical Mediators of Host-Microbe Interaction in the Gut. Annu. Rev. Microbiol 77, 479–497. 10.1146/annurev-micro-032421-111819. [PubMed: 37339735]
2. Li X, Zhang B, Hu Y, and Zhao Y (2021). New Insights Into Gut-Bacteria-Derived Indole and Its Derivatives in Intestinal and Liver Diseases. Front. Pharmacol 12, 769501. 10.3389/fphar.2021.769501. [PubMed: 34966278]
3. Roager HM, and Licht TR (2018). Microbial tryptophan catabolites in health and disease. Nat. Commun 9, 3294. 10.1038/s41467-018-05470-4. [PubMed: 30120222]
4. Agus A, Planchais J, and Sokol H (2018). Gut Microbiota Regulation of Tryptophan Metabolism in Health and Disease. Cell Host Microbe 23, 716–724. 10.1016/j.chom.2018.05.003. [PubMed: 29902437]
5. Ma Y, Liu X, and Wang J (2022). Small molecules in the big picture of gut microbiome-host cross-talk. EBioMedicine 81, 104085. 10.1016/j.ebiom.2022.104085. [PubMed: 35636316]
6. Ye X, Li H, Anjum K, Zhong X, Miao S, Zheng G, Liu W, and Li L (2022). Dual Role of Indoles Derived From Intestinal Microbiota on Human Health. Front. Immunol 13, 903526. 10.3389/fimmu.2022.903526. [PubMed: 35784338]
7. Dodd D, Spitzer MH, Van Treuren W, Merrill BD, Hryckowian AJ, Higginbottom SK, Le A, Cowan TM, Nolan GP, Fischbach MA, and Sonnenburg JL (2017). A gut bacterial pathway metabolizes aromatic amino acids into nine circulating metabolites. Nature 551, 648–652. 10.1038/nature24661. [PubMed: 29168502]
8. Lamas B, Richard ML, Leducq V, Pham H-P, Michel M-L, Da Costa G, Bridonneau C, Jegou S, Hoffmann TW, Natividad JM, et al. (2016). CARD9 impacts colitis by altering gut microbiota metabolism of tryptophan into aryl hydrocarbon receptor ligands. Nat. Med 22, 598–605. 10.1038/nm.4102. [PubMed: 27158904]
9. Zelante T, Iannitti RG, Cunha C, De Luca A, Giovannini G, Pieraccini G, Zecchi R, D'Angelo C, Massi-Benedetti C, Fallarino F, et al. (2013). Tryptophan Catabolites from Microbiota Engage Aryl Hydrocarbon Receptor and Balance Mucosal Reactivity via Interleukin-22. Immunity 39, 372–385. 10.1016/j.immuni.2013.08.003. [PubMed: 23973224]
10. Wlodarska M, Luo C, Kolde R, d'Hennezel E, Annand JW, Heim CE, Krastel P, Schmitt EK, Omar AS, Creasey EA, et al. (2017). Indoleacrylic Acid Produced by Commensal Peptostreptococcus

Author Manuscript Author Manuscript Author Manuscript Author Manuscript

Species Suppresses Inflammation. Cell Host Microbe 22, 25–37.e6. 10.1016/j.chom.2017.06.007. [PubMed: 28704649]

11. de Mello VD, Paananen J, Lindström J, Lankinen MA, Shi L, Kuusisto J, Pihlajamäki J, Auriola S, Lehtonen M, Rolandsson O, et al. (2017). Indolepropionic acid and novel lipid metabolites are associated with a lower risk of type 2 diabetes in the Finnish Diabetes Prevention Study. Sci. Rep 7, 46337. 10.1038/srep46337. [PubMed: 28397877]
12. Zhao Q, Chen T, Ni C, Hu Y, Nan Y, Lin W, Liu Y, Zheng F, Shi X, Lin Z, et al. (2022). Indole-3-propionic Acid Attenuates HI-Related Blood–Brain Barrier Injury in Neonatal Rats by Modulating the PXR Signaling Pathway. ACS Chem. Neurosci 13, 2897–2912. 10.1021/acschemneuro.2c00418. [PubMed: 36129348]
13. Parolisi S, Montanari C, Borghi E, Cazzorla C, Zuvadelli J, Tosi M, Barone R, Bensi G, Bonfanti C, Dionisi Vici C, et al. (2023). Possible role of tryptophan metabolism along the microbiota-gut-brain axis on cognitive & behavioral aspects in Phenylketonuria. Pharmacol. Res 197, 106952. 10.1016/j.phrs.2023.106952. [PubMed: 37804926]
14. Singh R, Zogg H, Wei L, Bartlett A, Ghoshal UC, Rajender S, and Ro S (2021). Gut Microbial Dysbiosis in the Pathogenesis of Gastrointestinal Dysmotility and Metabolic Disorders. J. Neurogastroenterol. Motil 27, 19–34. 10.5056/jnm20149. [PubMed: 33166939]
15. Bhattarai Y, Williams BB, Battaglioli EJ, Whitaker WR, Till L, Grover M, Linden DR, Akiba Y, Kandimalla KK, Zachos NC, et al. (2018). Gut Microbiota-Produced Tryptamine Activates an Epithelial G-Protein-Coupled Receptor to Increase Colonic Secretion. Cell Host Microbe 23, 775–785.e5. 10.1016/j.chom.2018.05.004. [PubMed: 29902441]
16. Tintelnot J, Xu Y, Lesker TR, Schönlein M, Konczalla L, Giannou AD, Pelczar P, Kylies D, Puelles VG, Bielecka AA, et al. (2023). Microbiota-derived 3-IAA influences chemotherapy efficacy in pancreatic cancer. Nature 615, 168–174. 10.1038/s41586-023-05728-y. [PubMed: 36813961]
17. Gong X, Zhang R, Wang J, and Yan Y (2022). Engineering of a TrpR-Based Biosensor for Altered Dynamic Range and Ligand Preference. ACS Synth. Biol 11, 2175–2183. 10.1021/acssynbio.2c00134. [PubMed: 35594503]
18. Amrofell MB, Rottinghaus AG, and Moon TS (2020). Engineering microbial diagnostics and therapeutics with smart control. Curr. Opin. Biotechnol 66, 11–17. 10.1016/j.copbio.2020.05.006. [PubMed: 32563763]
19. Rottinghaus AG, Amrofell MB, and Moon TS (2020). Biosensing in Smart Engineered Probiotics. Biotechnol. J 15, 1900319. 10.1002/biot.201900319.
20. Volk MJ, Tran VG, Tan S-I, Mishra S, Fatma Z, Boob A, Li H, Xue P, Martin TA, and Zhao H (2023). Metabolic Engineering: Methodologies and Applications. Chem. Rev 123, 5521–5570. 10.1021/acs.chemrev.2c00403. [PubMed: 36584306]
21. Rottinghaus AG, Xi C, Amrofell MB, Yi H, and Moon TS (2022). Engineering ligand-specific biosensors for aromatic amino acids and neurochemicals. Cell Syst 13, 204–214.e4. 10.1016/j.cels.2021.10.006. [PubMed: 34767760]
22. Xi C, Diao J, and Moon TS (2023). Advances in ligand-specific biosensing for structurally similar molecules. Cell Syst 14, 1024–1043. 10.1016/j.cels.2023.10.009. [PubMed: 38128482]
23. d'Oelsnitz S, Kim W, Burkholder NT, Javanmardi K, Thyer R, Zhang Y, Alper HS, and Ellington AD (2022). Using fungible biosensors to evolve improved alkaloid biosyntheses. Nat. Chem. Biol 18, 981–989. 10.1038/s41589-022-01072-w. [PubMed: 35799063]
24. d'Oelsnitz S, Diaz DJ, Kim W, Acosta DJ, Dangerfield TL, Schechter MW, Minus MB, Howard JR, Do H, Loy JM, et al. (2024). Biosensor and machine learning-aided engineering of an amaryllidaceae enzyme. Nat. Commun 15, 2084. 10.1038/s41467-024-46356-y. [PubMed: 38453941]
25. Chang H-J, Zúñiga A, Conejero I, Voyvodic PL, Gracy J, Fajardo-Ruiz E, Cohen-Gonsaud M, Cambray G, Pageaux G-P, Meszaros M, et al. (2021). Programmable receptors enable bacterial biosensors to detect pathological biomarkers in clinical samples. Nat. Commun 12, 5216. 10.1038/s41467-021-25538-y. [PubMed: 34471137]
26. Wan J, Peng W, Li X, Qian T, Song K, Zeng J, Deng F, Hao S, Feng J, Zhang P, et al. (2021). A genetically encoded sensor for measuring serotonin dynamics. Nat. Neurosci 24, 746–752. 10.1038/s41593-021-00823-7. [PubMed: 33821000]

Author Manuscript Author Manuscript Author Manuscript Author Manuscript

27. Marmorstein RQ, Joachimiak A, Sprinzl M, and Sigler PB (1987). The structural basis for the interaction between L-tryptophan and the Escherichia coli trp aporepressor. J. Biol. Chem 262, 4922–4927. 10.1016/S0021-9258(18)61285-2. [PubMed: 3549712]
28. Otwinowski Z, Schevitz RW, Zhang R-G, Lawson CL, Joachimiak A, Marmorstein RQ, Luisi BF, and Sigler PB (1988). Crystal structure of trp represser/operator complex at atomic resolution. Nature 335, 321–329. 10.1038/335321a0. [PubMed: 3419502]
29. Zhang R. -g, Joachimiak A, Lawson CL, Schevitz RW, Otwinowski Z, and Sigler (1987). The crystal structure of trp aporepressor at 1.8 Å shows how binding tryptophan enhances DNA affinity. Nature 327, 591–597. 10.1038/327591a0. [PubMed: 3600756]
30. Stiel AC, Shanmugaratnam S, Herud-Sikimic O, Jürgens G, and Höcker B (2020). Ligand promiscuity in the tryptophan repressor – from structural understanding towards rational design. Preprint at bioRxiv. 10.1101/2020.01.20.912972.
31. Herud-Sikimić O, Stiel AC, Kolb M, Shanmugaratnam S, Berendzen KW, Feldhaus C, Höcker B, and Jürgens G (2021). A biosensor for the direct visualization of auxin. Nature 592, 768–772. 10.1038/s41586-021-03425-2. [PubMed: 33828298]
32. Ellefson JW, Ledbetter MP, and Ellington AD (2018). Directed evolution of a synthetic phylogeny of programmable Trp repressors. Nat. Chem. Biol 14, 361–367. 10.1038/s41589-018-0006-7. [PubMed: 29483643]
33. Jumper J, Evans R, Pritzel A, Green T, Figurnov M, Ronneberger O, Tunyasuvunakool K, Bates R, Žídek A, Potapenko A, et al. (2021). Highly accurate protein structure prediction with AlphaFold. Nature 596, 583–589. 10.1038/s41586-021-03819-2. [PubMed: 34265844]
34. DeLuca S, Khar K, and Meiler J (2015). Fully Flexible Docking of Medium Sized Ligand Libraries with RosettaLigand. PLoS One 10, e0132508. 10.1371/journal.pone.0132508. [PubMed: 26207742]
35. Murooka Y, Doi N, and Harada T (1979). Distribution of membrane-bound monoamine oxidase in bacteria. Appl. Environ. Microbiol 38, 565–569. 10.1128/aem.38.4.565-569.1979. [PubMed: 120132]
36. Patten CL, Blakney AJC, and Coulson TJD (2013). Activity, distribution and function of indole-3-acetic acid biosynthetic pathways in bacteria. Crit. Rev. Microbiol 39, 395–415. 10.3109/1040841X.2012.716819. [PubMed: 22978761]
37. Dimopoulou C, Bongers M, Pedersen M, Bahl MI, Sommer MOA, Laursen MF, and Licht TR (2023). An engineered Escherichia coli Nissle 1917 increase the production of indole lactic acid in the gut. FEMS Microbiol. Lett 370, fnad027. 10.1093/femsle/fnad027. [PubMed: 37028942]
38. Smith E.a., and Macfarlane G.t. (1996). Enumeration of human colonic bacteria producing phenolic and indolic compounds: effects of pH, carbohydrate availability and retention time on dissimilatory aromatic amino acid metabolism. J. Appl. Bacteriol 81, 288–302. 10.1111/j.1365-2672.1996.tb04331.x. [PubMed: 8810056]
39. Friedlander T, Prizak R, Guet CC, Barton NH, and Tkačik G (2016). Intrinsic limits to gene regulation by global crosstalk. Nat. Commun 7, 12307. 10.1038/ncomms12307. [PubMed: 27489144]
40. Mirdita M, Schütze K, Moriwaki Y, Heo L, Ovchinnikov S, and Steinegger M (2022). ColabFold: making protein folding accessible to all. Nat. Methods 19, 679–682. 10.1038/s41592-022-01488-1. [PubMed: 35637307]
41. Evans R, O'Neill M, Pritzel A, Antropova N, Senior A, Green T, Žídek A, Bates R, Blackwell S, Yim J, et al. (2021). Protein complex prediction with AlphaFold-Multimer. Bioinformatics. 10.1101/2021.10.04.463034.
42. Lyskov S, Chou F-C, Conchúir SÓ, Der BS, Drew K, Kuroda D, Xu J, Weitzner BD, Renfrew PD, Sripakdeevong P, et al. (2013). Serverification of Molecular Modeling Applications: The Rosetta Online Server That Includes Everyone (ROSIE). PLoS One 8, e63906. 10.1371/journal.pone.0063906. [PubMed: 23717507]
43. Combs SA, DeLuca SL, DeLuca SH, Lemmon GH, Nannemann DP, Nguyen ED, Willis JR, Sheehan JH, and Meiler J (2013). Small-molecule ligand docking into comparative models with Rosetta. Nat. Protoc 8, 1277–1298. 10.1038/nprot.2013.074. [PubMed: 23744289]

Author Manuscript Author Manuscript Author Manuscript Author Manuscript

44. Zeng J, and Spiro S (2013). Finely Tuned Regulation of the Aromatic Amine Degradation Pathway in Escherichia coli. J. Bacteriol 195, 5141–5150. 10.1128/JB.00837-13. [PubMed: 24013633]
45. Xiao S, Wang Z, Wang B, Hou B, Cheng J, Bai T, Zhang Y, Wang W, Yan L, and Zhang J (2023). Expanding the application of tryptophan: Industrial biomanufacturing of tryptophan derivatives. Front. Microbiol 14, 1099098. 10.3389/fmicb.2023.1099098. [PubMed: 37032885]
46. Moon TS (2022). SynMADE: synthetic microbiota across diverse ecosystems. Trends Biotechnol 40, 1405–1414. 10.1016/j.tibtech.2022.08.010. [PubMed: 36117027]
47. Spaepen S, and Vanderleyden J (2011). Auxin and Plant-Microbe Interactions. Cold Spring Harb. Perspect. Biol 3, a001438. 10.1101/cshperspect.a001438. [PubMed: 21084388]
48. Duca D, Lorv J, Patten CL, Rose D, and Glick BR (2014). Indole-3-acetic acid in plant–microbe interactions. Antonie Leeuwenhoek 106, 85–125. 10.1007/s10482-013-0095-y. [PubMed: 24445491]
49. Opitz CA, Somarribas Patterson LF, Mohapatra SR, Dewi DL, Sadik A, Platten M, and Trump S (2020). The therapeutic potential of targeting tryptophan catabolism in cancer. Br. J. Cancer 122, 30–44. 10.1038/s41416-019-0664-6. [PubMed: 31819194]
50. Mehrer CR, Incha MR, Politz MC, and Pfleger BF (2018). Anaerobic production of medium-chain fatty alcohols via a b-reduction pathway. Metab. Eng 48, 63–71. 10.1016/j.ymben.2018.05.011. [PubMed: 29807110]
51. Roh JH, Suzuki H, Azakami H, Yamashita M, Murooka Y, and Kumagai H (1994). Purification, Characterization, and Crystallization of Monoamine Oxidase from *Escherichia coli* K-12. Biosci. Biotechnol. Biochem 58, 1652–1656. 10.1271/bbb.58.1652. [PubMed: 7765483]
52. Jiménez J, Doerr S, Martínez-Rosell G, Rose AS, and De Fabritiis G (2017). DeepSite: protein-binding site predictor using 3D-convolutional neural networks. Bioinformatics 33, 3036–3042. 10.1093/bioinformatics/btx350. [PubMed: 28575181]
53. Kothiwale S, Mendenhall JL, and Meiler J (2015). BCL::Conf: small molecule conformational sampling using a knowledge based rotamer library. J. Cheminform 7, 47. 10.1186/s13321-015-0095-1. [PubMed: 26473018]

Author Manuscript Author Manuscript Author Manuscript Author Manuscript

Highlights

- Microbial sensor development for tryptophan or auxin metabolites
- Generalizable ligand-specificity enhancement in transcriptional factors
- Structural analysis pipeline for the identification of allosteric mechanisms
- Biosensing repertoire extension with swappable enzyme and regulator modules

Author Manuscript Author Manuscript Author Manuscript Author Manuscript

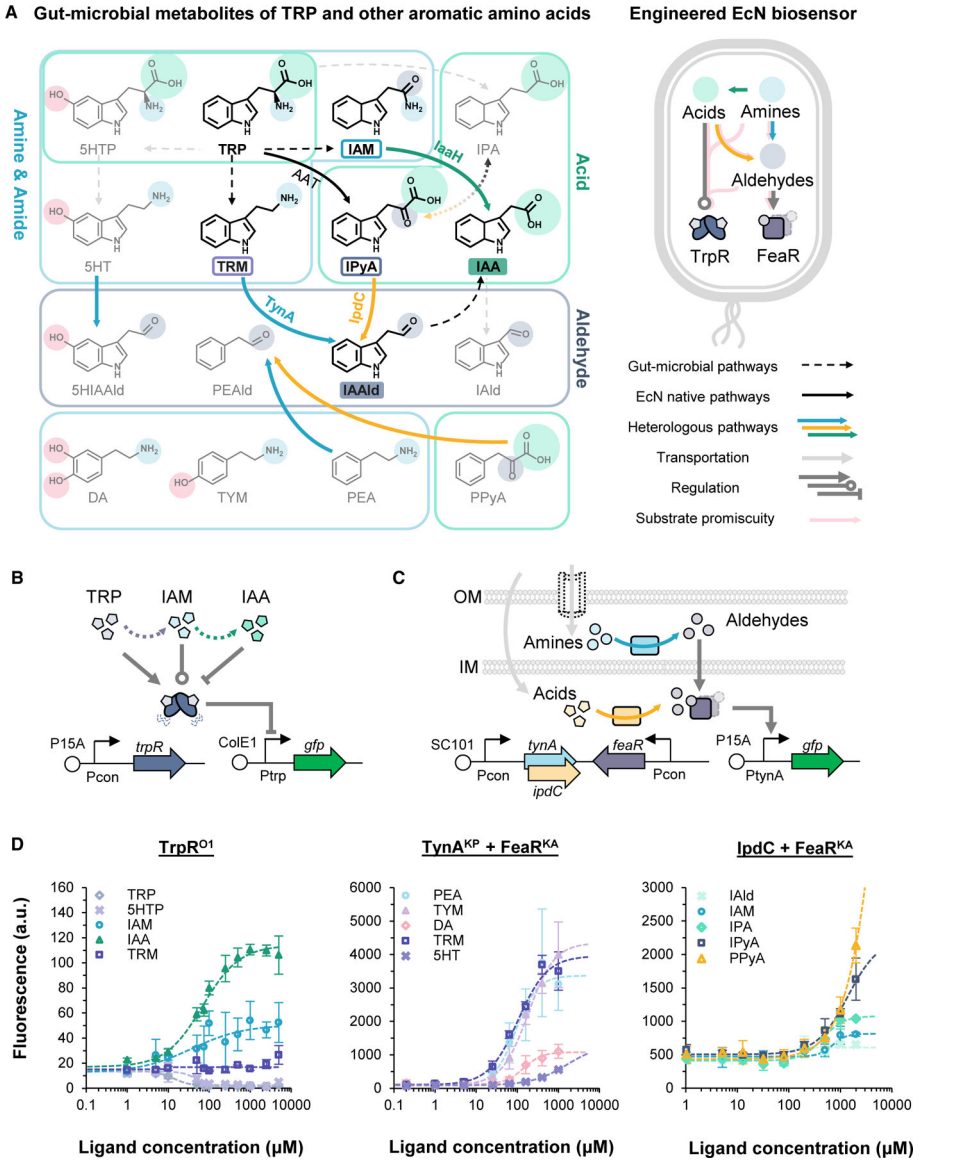

Figure 1. Characterization of nonspecific transcriptional biosensors for gut-microbial tryptophan metabolite detection

(A) Biosynthetic pathways of IAA (in black) and other indole derivatives (in gray) in *E. coli* Nissle 1917 (EcN) and other gut microbes. IAM, TRM, and IPyA pathways are considered major microbial IAA biosynthesis pathways. IAAld and IAA are the targeted effectors of the evolved FeaR and TrpR regulators in this study.

(B) Schematic of the TrpR biosensor regulated by TRP metabolites, with the substrate (TRP), intermediate (IAM), and product (IAA) of the IAA biosynthesis differentially regulating the TrpR regulator.

(C) Schematics of TynA-FeaR and IpdC-FeaR biosensors regulated by aromatic amines and acids. The enzyme module converts substrates to aldehydes, activating the FeaR regulator to bind the PtynA promoter and induce gene expression.

(D) Transfer curves for three sensor systems with plasmid-based overexpression of (left) $TrpR^{O1}$, (middle) $TynA^{KP}$ + $FeaR^{KA}$, and (right) IpdC + $FeaR^{KA}$ in response to increasing

Author Manuscript Author Manuscript Author Manuscript Author Manuscript

concentrations of TRP analogs. “KP,” *K. pneumoniae*; “KA,” *K. aerogenes*. Values and error bars correspond to the mean ± SD of three biological replicates ($n = 3$).
Ligands: 5HTP, 5-hydroxy-L-tryptophan; TRP, L-tryptophan; IPA, indole-3-propionic acid; IPyA, indole-3-pyruvic acid; IAA, indole-3-acetic acid; 5HT, 5-hydroxytryptamine; TRM, tryptamine; DA, dopamine; TYM, tyramine; PEA, phenethylamine; IAM, indole-3-acetamide; IAld, indole-3-carboxaldehyde; IAAld, indole-3-acetaldehyde; 5HIAAld, 5-hydroxyindole acetaldehyde; PEAld, phenylacetaldehyde; PPyA, phenylpyruvic acid.
Enzymes: AAT, aromatic amino acid aminotransferase; IaaH, indole-3-acetamide hydrolase; IpdC, indole-3-pyruvate decarboxylase; TynA, tyramine oxidase.

Author Manuscript Author Manuscript Author Manuscript Author Manuscript

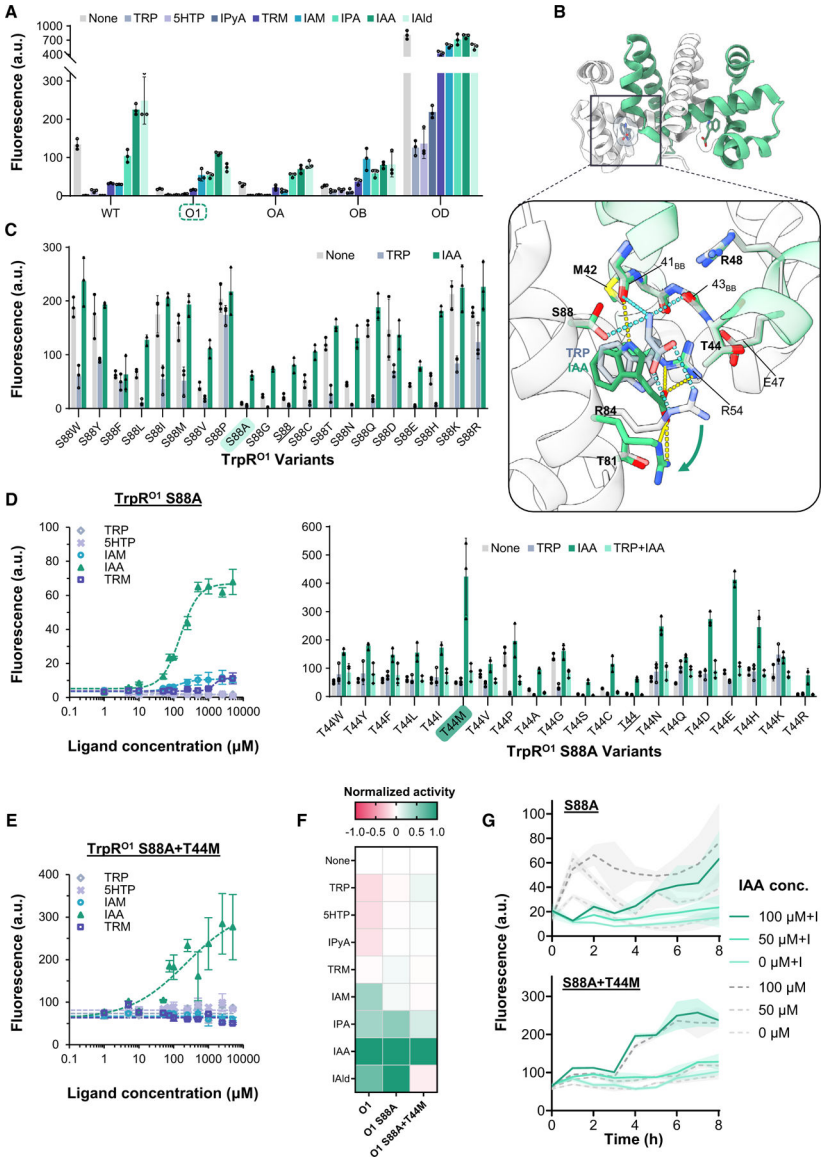

Figure 2. Evolution of the TrpR regulator for IAA-specific biosensing

(A) Comparative activity of Ptrp wild type (WT), O1, OA, OB, or OD regulated by cognate TrpR variants after 8 h of induction with 1 mM TRP analogs.

(B) Structural analysis of wild-type TrpR crystal structure in complex with IAA (PDB: 6EJW) and TRP (PDB: 2OZ9) to reveal the key residues influencing ligand-specific interactions. Crystal structures of $TrpR^{WT}$ bound with IAA (in dark green) or TRP (in transparent gray) are aligned to each other. The backbone of the IAA-binding TrpR dimer is presented with one chain in gray and the other in green. IAA-binding residues are shown in green with hydrogen bond in yellow. TRP-binding residues are in gray with hydrogen bonds in cyan. Mutagenesis-targeted residues are in boldface.

(C) Fluorescence from $Ptrp^{O1}$ regulated by $TrpR^{O1}$ variants with 20 different substitutions at residue 88 after 8 h of induction with 0.5 mM TRP or IAA.

Author Manuscript Author Manuscript Author Manuscript Author Manuscript

(D) (Left) Transfer curves of the IAA-selective sensor in response to increasing concentrations of indole derivatives. (Right) Fluorescence from $Ptrp^{O1}$ regulated by $TrpR^{O1}$ S88A mutants at residue 44 after 8 h of induction with 0.5 mM TRP, 0.5 mM IAA, or a mixture of both (Mix).

(E) Transfer curves of the IAA-specific TrpR sensor in response to increasing concentrations of indole derivatives.

(F) Cross-reactivity profiles of TrpR-based IAA sensor variants against various indole derivatives. Values on the heatmap represent the fluorescence response after 8 h of induction with 1 mM ligands, normalized to each variant's IAA activity.

(G) Time-course fluorescent response of the IAA-selective and specific sensor to escalating concentrations of IAA with (solid line) or without (dashed line) interfering molecules. I represents a mixture of ten selected TRP analogs, each at 10 μM, without IAA, Tyra, or PEA.

Values and error bars correspond to the mean ± SD of three biological replicates ($n = 3$). See also Figures S1–S5.

Author Manuscript Author Manuscript Author Manuscript Author Manuscript

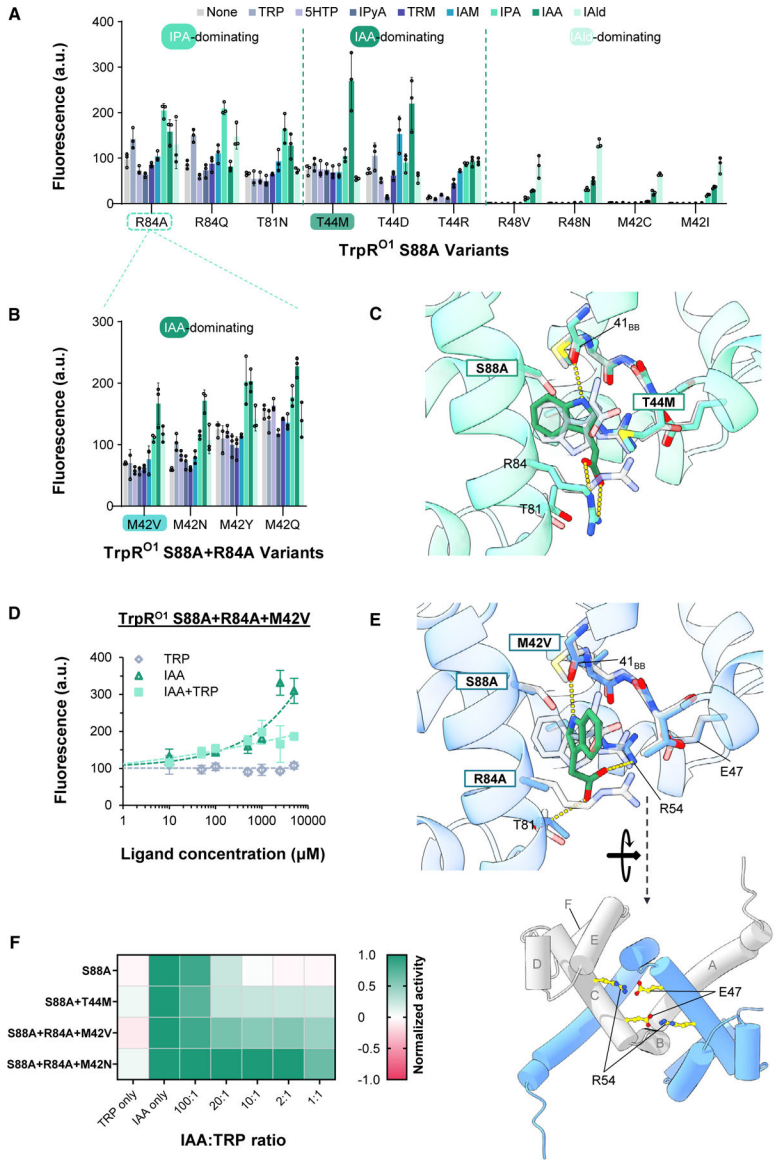

Figure 3. Manipulating the dimerization of TrpR regulators to alter the ligand selectivity

(A) Comparative activity of $Ptrp^{O1}$ regulated by selected variants based on $TrpR^{O1}$ S88A after 8 h of induction with 1 mM various TRP analogs. Mutations at M42 and R48 maintain a low basal level of fluorescence, with IAld as the dominant effector. Mutations at T81 and R84 increase basal-level fluorescence, with IPA as the dominant effector. Mutations at T44 display variations in basal-level fluorescence with IAA as the dominant effector.

(B) Restoration of IAA-dominating effector preference in TrpR through mutations at residue 42 from $TrpR^{O1}$ S88A + R84A.

(C) Molecular modeling of $TrpR^{O1}$ S88A + T44M depicting the impact of mutations at S88 and T44 on ligand selectivity. The crystal structure of wild-type TrpR binding with TRP (in transparent gray) and the predicted structure of $TrpR^{O1}$ S88A + T44M binding with IAA (in dark green) are aligned. The IAA-bound TrpR's backbone is presented in green.

Author Manuscript Author Manuscript Author Manuscript Author Manuscript

IAA-binding residues are shown in green with hydrogen bonds in yellow. TRP-binding residues are shown in gray. Mutations are labeled.

(D) Transfer curves of a $TrpR^{O1}$ S88A + R84A + M42V displaying the ligand preference for IAA over TRP.

(E) Molecular modeling of $TrpR^{O1}$ S88A + R84A + M42V depicting the impact of mutations at S88, R84, and M42 on ligand selectivity. (Top) The crystal structure of wild-type TrpR binding with TRP (in transparent gray) and the predicted structure of $TrpR^{O1}$ S88A + R84A + M42V binding with IAA (in dark green) are aligned. The IAA-bound TrpR's backbone is presented in blue. IAA-binding residues are shown in blue with hydrogen bonds in yellow. TRP-binding residues are shown in gray. Mutations are labeled. (Bottom) The R54-E47 (in yellow) coplanar salt bridge is disrupted by the binding of IAA to R54. Two chains of $TrpR^{O1}$ S88A + R84A + M42V dimer are shown in white and blue.

(F) Elimination of TRP cross-reactivity in the presence of IAA. Values on the heatmap reflect each variant's fluorescence response induced by 1 mM IAA with varying concentrations of TRP (0, 10, 100, and 1,000 μM) normalized to 1 mM IAA (IAA only) condition.

Values and error bars correspond to the mean ± SD of three biological replicates ($n = 3$). See also Figures S5–S8.

Author Manuscript Author Manuscript Author Manuscript Author Manuscript

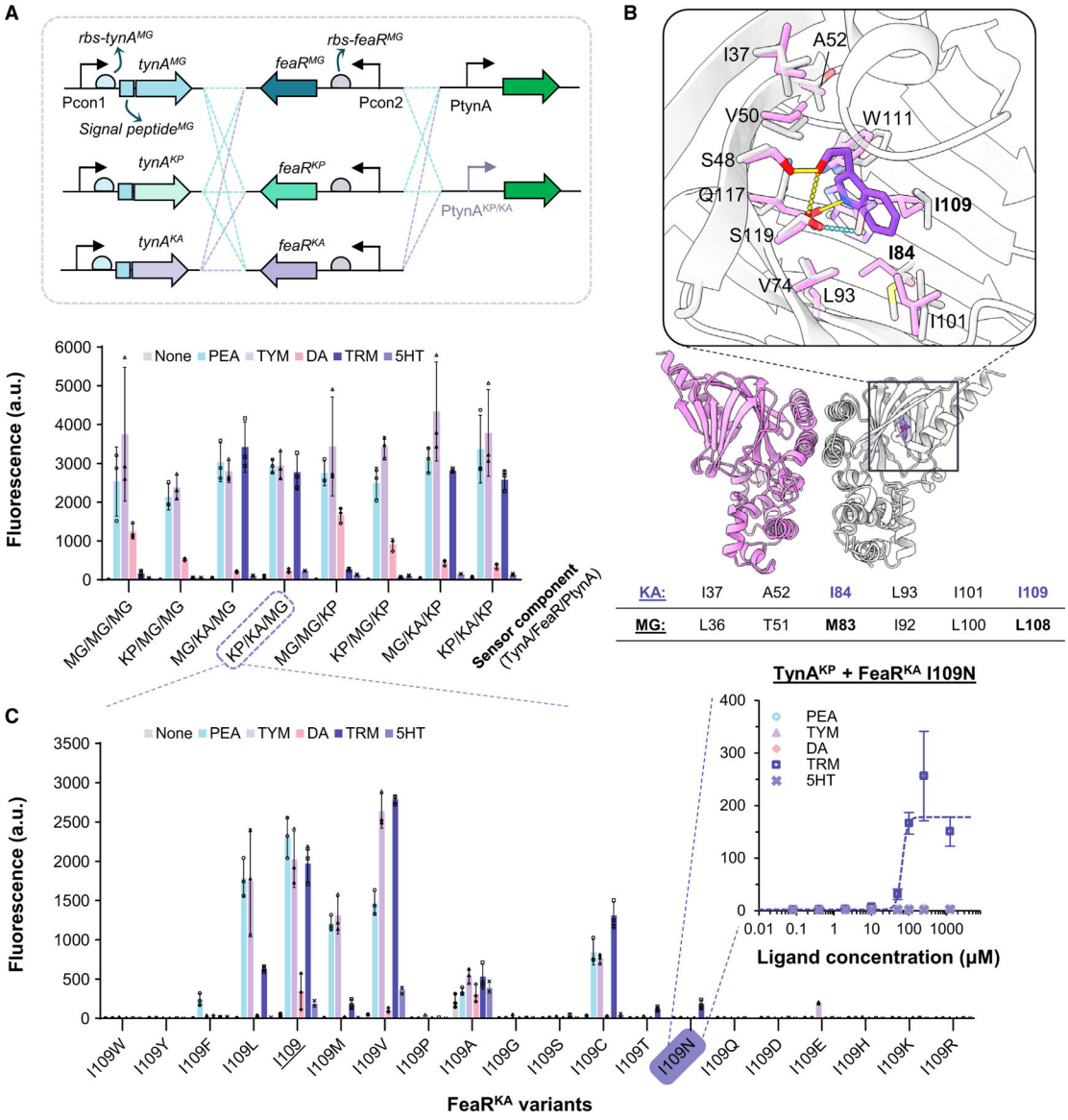

Figure 4. Engineering TynA-FeaR homologs and mutagenesis libraries to identify TRM-specific sensors

(A) (Top) Component optimization for enhanced TRM detection. Biosensors were constructed by combining PtynA, *tynA*, and *feaR* from *E. coli* MG1655 (MG), *K. pneumoniae* (KP), and *K. aerogenes* (KA) to achieve varied ligand selectivity. (Bottom) Comparative activity of TRM sensor candidates with different component configurations after 24 h of induction with 0.5 mM ligands.

(B and C) (B) Molecular modeling of $FeaR^{KA}$ dimer elucidating the impact of mutations on IAAld selectivity. Predicted structures of $FeaR^{MG}$ and $FeaR^{KA}$ dimer in complex with IAAld are aligned. Two chains of $FeaR^{KA}$ are shown in pink and gray. IAAld-binding residues in $FeaR^{KA}$ are shown in pink with hydrogen bonds in yellow, and those in $FeaR^{MG}$ are in gray with hydrogen bonds in cyan. Sequence mismatches in $FeaR^{KA}$ and $FeaR^{MG}$ ligand-binding pockets are detailed in an accompanying table, with important residues determining ligand selectivity in bold. (C) (Left) Fluorescence from PtynA regulated by

Author Manuscript Author Manuscript Author Manuscript Author Manuscript

TynA^{KP} and FeaR^{KA} variants with 20 different substitutions at residue 109 after 24 h of induction with 0.5 mM ligands. (Right) Transfer curves of the TRM-specific sensor after 24 h of induction with escalating concentrations of five amines.

Values and error bars correspond to the mean ± SD of three biological replicates (n = 3). See also Figures S9–S12.

Author Manuscript Author Manuscript Author Manuscript Author Manuscript

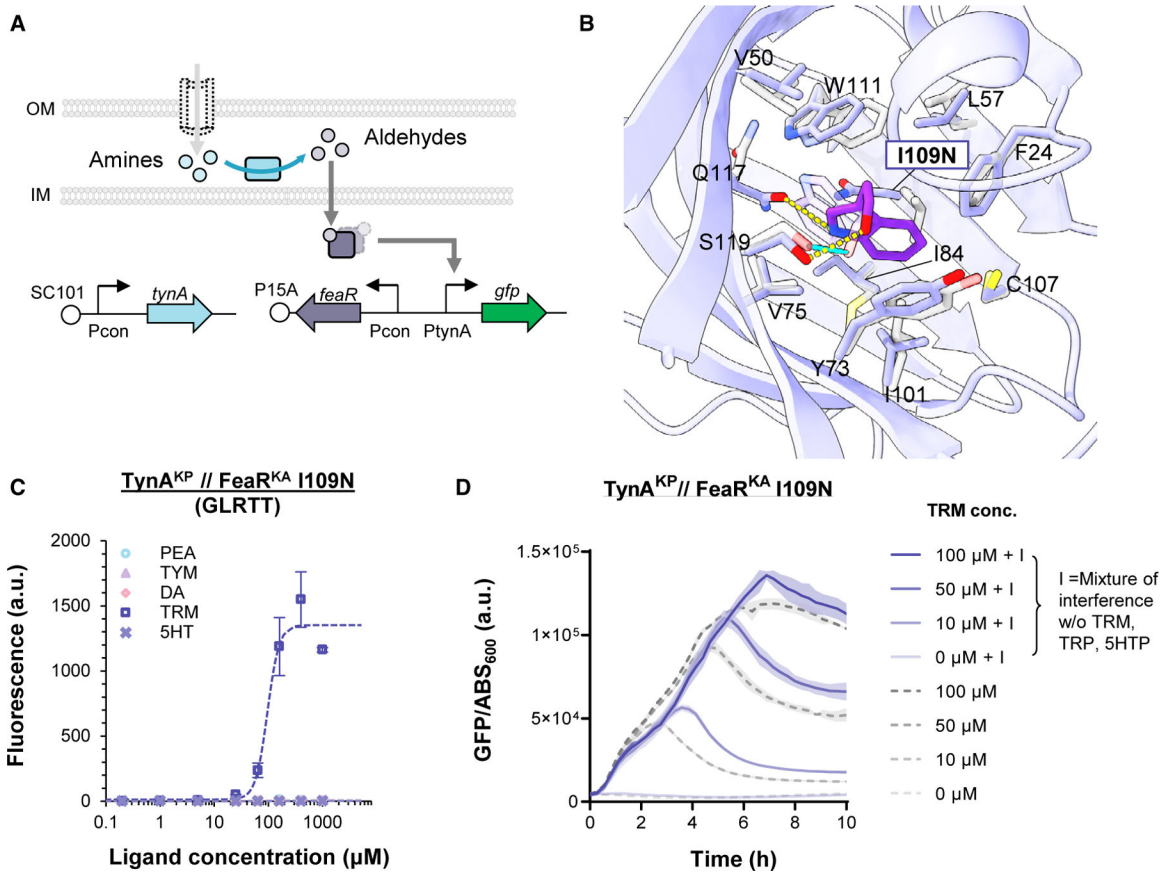

Figure 5. Enhancing TRM-specific biosensor performance

(A) Schematic of TynA-FeaR-based biosensor system featuring an elevated expression of FeaR.

(B) Molecular modeling of FeaR^{KA} I109N elucidating the impact of I109N mutation. Predicted structures of FeaR^{MG} and FeaR^{KA} I109N in complex with IAAld are aligned. The backbone of FeaR^{KA} I109N is shown in violet. IAAld-binding residues in FeaR^{KA} are highlighted in violet with yellow hydrogen bonds, and those in FeaR^{MG} are in gray with cyan hydrogen bonds.

(C) Transfer curves of the TRM-specific sensor with an elevated expression of FeaR^{KA} I109N, tested in M9 glycerol medium supplemented with thiamine and trace elements (GLRTT).

(D) Kinetic fluorescence response of the TRM-specific sensor to escalating TRM concentrations with (solid line) or without (dashed line) a background of ten selected TRP analogs, each at 10 μM.

Values and error bars correspond to the mean ± SD of three biological replicates (n = 3). See also Figures S11–S13.

Author Manuscript Author Manuscript Author Manuscript Author Manuscript

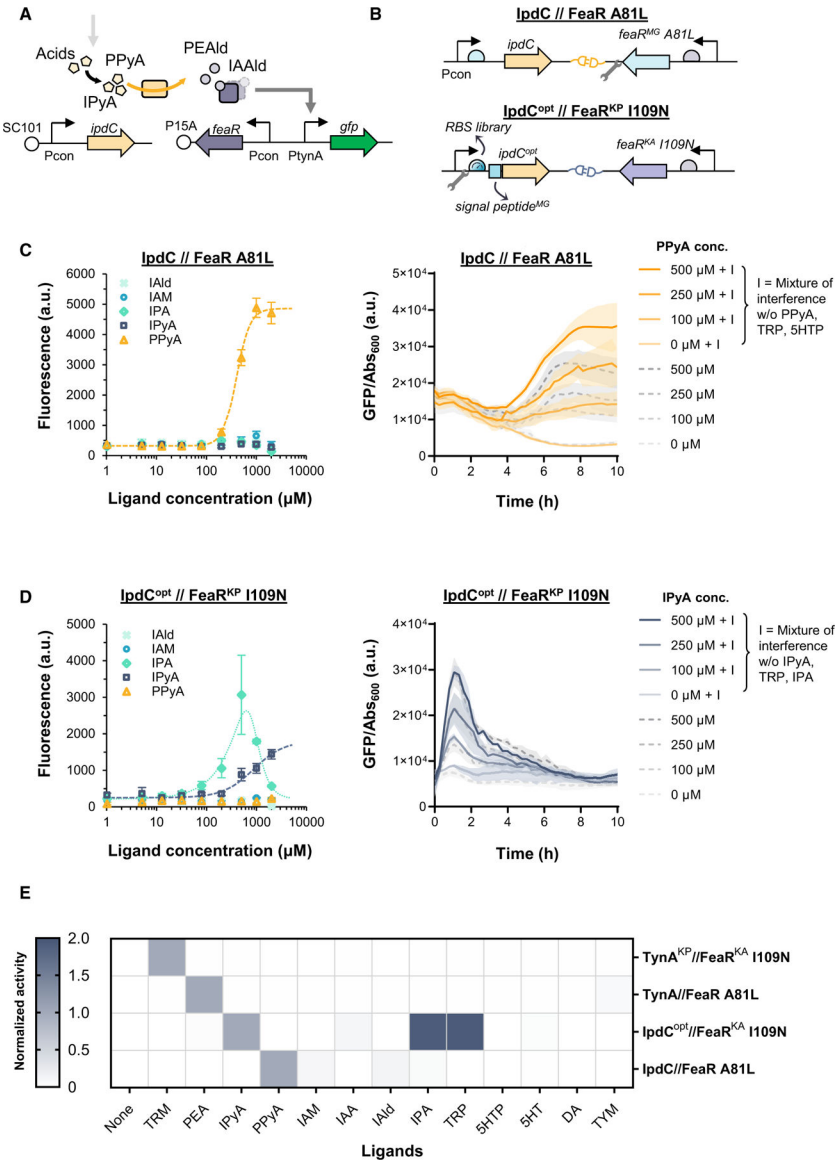

Figure 6. Expanding the detection scope of FeaR-based biosensors by a plug-and-play strategy

(A) Schematic of IpdC-FeaR-based biosensor system featuring an elevated expression of FeaR.

(B) Tailoring IpdC expression and swapping FeaR variants to alter substrate specificity. A signal peptide of TynA from *E. coli* MG1655 (MG) is fused to IpdC for relieving aldehyde accumulation in cytoplasm, and a ribosome-binding site library is screened for optimized IpdC expression (IpdC^{opt}).

(C) (Left) Response curves of the PPyA-specific sensor after 24 h of induction with increasing concentrations of ligands. (Right) Kinetic fluorescence response of the PPyA-specific sensor to varying concentrations of PPyA in the presence (solid line) and absence (dashed line) of a mixture of ten selected TRP analogs, each at 10 μM.

(D) (Left) Response curves of the IPyA-targeted sensor after 24 h of induction with increasing concentrations of ligands. (Right) Kinetic fluorescence response of the IPyA-

Author Manuscript Author Manuscript Author Manuscript Author Manuscript

targeted sensor to varying concentrations of IPyA in the presence (solid line) and absence (dashed line) of a mixture of ten selected TRP analogs, each at 10 μM.

(E) Orthogonality matrix of FeaR-based biosensors for targeted substrates IPyA, PPyA, TRM, and PEA. Values on the heatmap represent the fluorescence response after 24 h of induction with 0.5 mM ligands, normalized to the activity induced by each sensor's target ligand.

Values and error bars correspond to the mean ± SD of three biological replicates ($n = 3$). See also Figures S14 and S15.